




Cite this: *Catal. Sci. Technol.*, 2024,  
14, 4256

# Ampere-level oxygen evolution reaction driven by $\text{Co}_3\text{O}_4$ nanoparticles supported on layered $\text{TiO}_2$ †

Hong Tang, <sup>a</sup> Wei Wu, <sup>a</sup> Takahiro Kojima, <sup>a</sup> Kenji Kazumi, <sup>b</sup>  
Kazuhiro Fukami <sup>b</sup> and Hiroshi Sakaguchi <sup>\*a</sup>

Cobalt oxide ( $\text{Co}_3\text{O}_4$ ) is an attractive catalyst for the oxygen evolution reaction (OER). However, the OER performance of previously reported  $\text{Co}_3\text{O}_4$  nanoparticles is insufficient for ampere-level current. The reason is the lack of covalent bonds between  $\text{Co}_3\text{O}_4$  nanoparticles and the substrate, which leads to a high electron transfer energy barrier. Herein,  $\text{Co}_3\text{O}_4$  nanoparticles supported on a layered  $\text{TiO}_2$  surface ( $\text{Co}_3\text{O}_4$ @layered- $\text{TiO}_2$ ) by Co–O–Ti covalent bonds are carefully constructed through the MXene precursor method. As a result,  $\text{Co}_3\text{O}_4$ @layered- $\text{TiO}_2$  exhibits brilliant OER performance with ultra-low potential (1.52 V to reach 100  $\text{mA cm}^{-2}$ ), ampere-level current density (1.66 V to reach 1000  $\text{mA cm}^{-2}$ ) and long-term durability (110 h at 500  $\text{mA cm}^{-2}$ ). Density functional theory studies have confirmed that the Co–O–Ti covalent bonds can adjust the d band center to optimize reaction energy barriers. This result illuminates a new strategy for constructing highly active materials on the metal oxide substrate for efficient electrocatalysis.

Received 30th April 2024,  
Accepted 8th June 2024

DOI: 10.1039/d4cy00557k

rsc.li/catalysis

## 1. Introduction

Hydrogen is the most promising future clean energy source, and electrochemical water splitting using electrolyzers is a crucial way to produce hydrogen gas efficiently.<sup>1–5</sup> Regarding the evolution reaction of hydrogen gas, the slow kinetics of the oxygen evolution reaction (OER) limits the water splitting ability, which causes electrolysis through a thermodynamically energy-unfavored process.<sup>6–8</sup> The intrinsic dilemma in the OER process is that after the intermediate (OH) is deprotonated to form  $\text{O}^*$ , an O–O bond needs to be formed in the next step, which limits the reaction kinetics.<sup>9–11</sup> The slow kinetics of the OER originating from the high reaction energy barrier causes massive energy consumption during the water-splitting process. Therefore, lowering the reaction energy barrier to achieve fast reaction kinetics is required to realize the efficient OER.<sup>12</sup>

In contrast with noble metal oxides, cobalt oxide ( $\text{Co}_3\text{O}_4$ ), as first-row 3d transition metal oxides with high abundance and low cost, have attracted widespread attention as alternative catalysts for the OER.<sup>13–16</sup> Yang *et al.* reported that  $\text{Co}_3\text{O}_4$  nanoparticles binding to the exfoliated few-layer 2D

$\text{Ti}_3\text{C}_2$  MXene nanosheets through electrostatic force exhibit the overpotential of 300 mV at a current density of 10  $\text{mA cm}^{-2}$  in basic solutions.<sup>17</sup> However, due to the interfacial electrostatic interaction between  $\text{Co}_3\text{O}_4$  nanoparticles and  $\text{Ti}_3\text{C}_2$  MXene, its OER performance suffers from the ampere-level current. In order to obtain an electrocatalyst that meets the requirements of ampere-level current, it is essential to enhance the activity of the catalyst by reducing the overpotential. It is effective to regulate the electronic properties of the active sites to reduce overpotential. One way to achieve ampere-level OER performance is to alter the electronic properties of active sites by covalently bonding them to a substrate.<sup>18–24</sup> Wang *et al.* reported that  $\text{WO}_3$  as the substrate to bind Ir nanoparticles through Ir–O–W bonds exhibits excellent catalytic ability for hydrogen evolution.<sup>23</sup> This result demonstrates that the formation of metal–oxygen covalent bonds is crucial for enhancing catalytic activity by tuning the free energy barrier for intermediates. Titanium dioxide ( $\text{TiO}_2$ ) is widely used as the substrate for loading active sites due to its exceptional chemical stability and durability.<sup>25,26</sup>

In this work,  $\text{TiO}_2$  with a two-dimensional (2D) layered structure as a substrate to support  $\text{Co}_3\text{O}_4$  nanoparticles with Co–O–Ti covalent bonds was constructed towards the efficient OER (Fig. 1). In here, the MXene precursor method is adopted, that is, loading cobalt ions onto the surface of layered  $\text{Ti}_3\text{C}_2$  MXene (obtained by etching  $\text{Ti}_3\text{AlC}_2$ ), then converting them into cobalt oxide and titanium dioxide by annealing at low temperatures in the air. During the

<sup>a</sup> Institute of Advanced Energy, Kyoto University, Kyoto 611-0011, Japan.

E-mail: sakaguchi@iae.kyoto-u.ac.jp

<sup>b</sup> Department of Materials Science and Engineering, Kyoto University, Kyoto 606-8501, Japan† Electronic supplementary information (ESI) available. See DOI: <https://doi.org/10.1039/d4cy00557k>

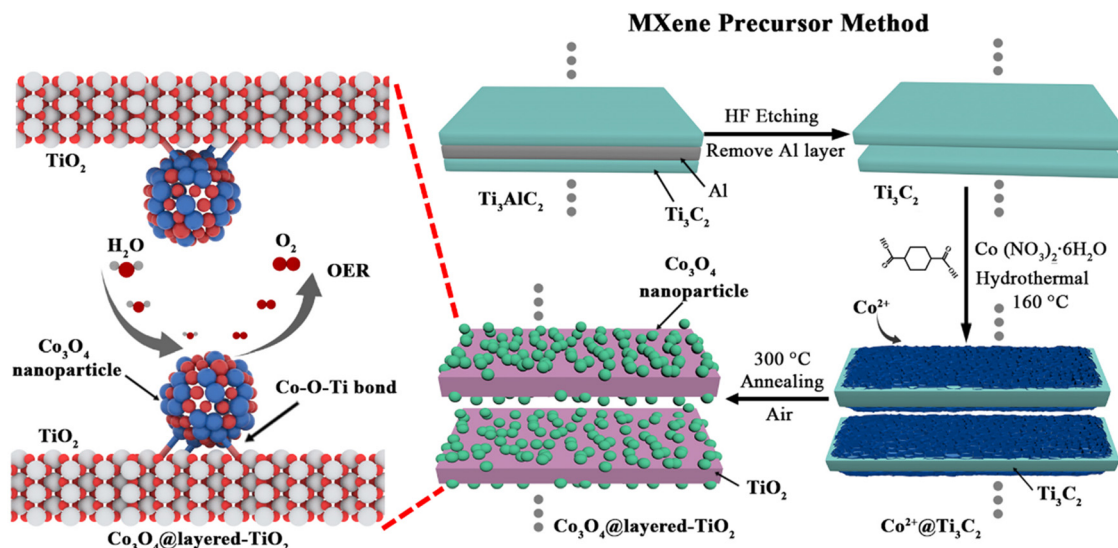


Fig. 1 Schematic illustration of the synthesis process of  $\text{Co}_3\text{O}_4@\text{layered-TiO}_2$  towards the OER.

annealing process, the cobalt precursor ( $\text{Co}^{2+}$ ) on the surface of the layered  $\text{Ti}_3\text{C}_2$  MXene is converted into  $\text{Co}_3\text{O}_4$ , while the  $\text{Ti}_3\text{C}_2$  MXene is oxidized into  $\text{TiO}_2$  to form Co–O–Ti covalent bonds. As a result, the  $\text{Ti}_3\text{C}_2$  MXene-derived  $\text{Co}_3\text{O}_4@\text{layered-TiO}_2$  composites exhibit brilliant OER performance with ultra-low potential, ampere-level current density and long-term durability. Density functional theory (DFT) studies have confirmed that the Co–O–Ti covalent bonds between  $\text{Co}_3\text{O}_4$  and  $\text{TiO}_2$  can adjust the d-band center to optimize the reaction energy barrier for reaction intermediates.

## 2. Experimental

### 2.1 Preparation of layered $\text{Ti}_3\text{C}_2$ MXene

$\text{Ti}_3\text{C}_2$  MXene was prepared by selectively etching  $\text{Ti}_3\text{AlC}_2$  with stirring. First, 3.0 g of  $\text{Ti}_3\text{AlC}_2$  powder was added to 60 mL of 40% hydrofluoric acid solution to remove the Al layer by maintaining it at  $60\text{ }^\circ\text{C}$  for 48 hours. Afterward, the strongly acidic  $\text{Ti}_3\text{C}_2$  MXene dispersion was centrifuged several times to obtain a neutral  $\text{Ti}_3\text{C}_2$  MXene dispersion. Finally, the layered  $\text{Ti}_3\text{C}_2$  was obtained by filtration and vacuum drying.

### 2.2 Preparation of $\text{Co}_3\text{O}_4@\text{layered-TiO}_2$

Firstly, 40 mg  $\text{Ti}_3\text{C}_2$  MXene, 145 mg  $\text{Co}(\text{NO}_3)_2 \cdot 6\text{H}_2\text{O}$  (0.50 mmol) and 76 mg (0.50 mmol) trans-1,4-cyclohexanedicarboxylic acid were ultrasonically dispersed in 30 mL of *N,N'*-dimethylformamide (DMF) for 30 min. Then, the obtained dispersion solution was transferred to a 50 mL autoclave reactor to be maintained at  $160\text{ }^\circ\text{C}$  for 16 hours in an oven. After cooling to room temperature, the black precipitate was dried overnight in a vacuum oven at  $60\text{ }^\circ\text{C}$ , followed by washing with ethanol and deionized water. Finally,  $\text{Co}_3\text{O}_4@\text{layered-TiO}_2$  was obtained by annealing the above sample at  $300\text{ }^\circ\text{C}$  for 2 h with a heating rate of  $2\text{ }^\circ\text{C min}^{-1}$  in the atmosphere.  $\text{Co}_3\text{O}_4$  was prepared using the same method, but without the addition of  $\text{Ti}_3\text{C}_2$  MXene. The

layered- $\text{TiO}_2$  was obtained by direct annealing  $\text{Ti}_3\text{C}_2$  MXene in a tube furnace at a heating rate of  $2\text{ }^\circ\text{C min}^{-1}$  at  $300\text{ }^\circ\text{C}$  for 2 h in an air gas atmosphere.

### 2.3 Material characterization

The morphology of the sample was observed using scanning electron microscopy (SEM) (JEOL, JSM-6500F) and high-resolution transmission electron microscopy (TEM) (JEOL, JEM-2100). Elemental mapping images were obtained using TEM (JEOL, JEM2100). The selective area electron diffraction (SAED) was performed by AC-TEM (FEI Titan, G2 60-300). The X-ray diffraction (XRD) spectra were obtained using a D/Max-III X-ray spectrometer (Panalytical, Philips X'Pert Pro) with  $\text{Cu K}\alpha$  radiation in the  $2\theta$  range of  $5^\circ$  to  $80^\circ$ . The X-ray photoelectron spectroscopy (XPS) was examined by using electron energy dispersive spectroscopy (JEOL, JPS-9010TRX).

### 2.4 Electrochemical measurements

The electrochemical performance tests of all catalysts were conducted using an electrochemical workstation (Solartron, SI1287) in an electrolytic cell with a three-electrode system. The alkaline electrolyte is 1.0 M KOH solution, the platinum plate electrode was used as the counter electrode, and a Hg/HgO electrode was used as the reference electrode. The  $\text{Co}_3\text{O}_4@\text{layered-TiO}_2$  electrode is obtained by the drop-dry method: 5 mg of the  $\text{Co}_3\text{O}_4@\text{layered-TiO}_2$  catalyst was first dispersed in a mixed solution of 500  $\mu\text{L}$  water, 450  $\mu\text{L}$  isopropyl alcohol and 50  $\mu\text{L}$  Nafion dispersion. Afterward, 40  $\mu\text{L}$  of the  $\text{Co}_3\text{O}_4@\text{layered-TiO}_2$  catalyst dispersion was dropped evenly on the carbon paper electrode with an area of  $0.5 \times 0.5\text{ cm}^2$ , then was used to test the electrochemical performance after drying. The potential relative to a reversible hydrogen electrode (RHE) under alkaline conditions was calculated by  $E_{\text{RHE}} = E_{\text{Hg/HgO}} + 0.098 + 0.0591 \times \text{pH}$ . Polarization curves were measured by linear sweep



voltammetry (LSV) at a sweep rate of  $5 \text{ mV s}^{-1}$ . The stability measurements were performed using galvanostatic testing at a current density of  $500 \text{ mA cm}^{-2}$ . Electrochemical impedance spectroscopy (EIS) was tested from the 10 000 to 0.1 Hz frequency range with an amplitude of 5 mV. The Tafel slope was obtained by  $\eta = b \times \log|j| + a$ , where  $\eta$ ,  $b$  and  $j$  are the potential, Tafel slope and the measured current density, respectively. The electrochemical double layer capacitance ( $C_{dl}$ ) was obtained by cyclic voltammetry (CV) measurements at a voltage of 0.25–0.35 V versus Hg/HgO.

## 2.5 Calculation methods

All DFT calculations were performed using the CASTEP simulation package in the Materials Studio software (BIOVIA, Materials Studio). The projector-augmented wave (PAW) method is used to describe the interactions between ion cores and valence electrons. The Perdew–Burke–Ernzerhof (PBE) functional and the generalized gradient approximation (GGA) were performed to describe exchange–correlation interaction calculation. The energy cutoff was set to 500 eV for geometry optimization and energy calculations of the lattice cells. The convergence accuracy of the electronic step is  $10^{-7}$  eV. The model was constructed by putting the  $\text{Co}_3\text{O}_4$  crystal on the  $\text{TiO}_2$  crystal. A vacuum of 20 Å thickness is added in the  $Z$  direction to avoid spurious interactions between periodic lattices. After optimizing the structural

model, the Co atom was chosen as the adsorption site to calculate the adsorption energy. The final enthalpy was obtained by optimizing the structure of the model. Finally, the adsorption energy ( $E_{\text{ads}}$ ) was calculated by  $\Delta E_{\text{ads}} = E_{\text{ad/sub}} - E_{\text{ad}} - E_{\text{sub}}$ , where  $E_{\text{ad/sub}}$ ,  $E_{\text{ad}}$ , and  $E_{\text{sub}}$  are the final enthalpy of the optimized adsorbate with the substrate system, adsorbate, and substrate, respectively. The free energy ( $\Delta G$ ) was calculated by  $\Delta G = \Delta E_{\text{ads}} + \text{ZPE} - T\Delta S$ , where ZPE is the zero-point energy and  $T\Delta S$  is the entropic contribution. The d band center ( $\epsilon_d$ ) for d orbital projected density of states (PDOS) of Ru can be calculated by the following equation:

$$\mu = \frac{\sum_b \epsilon N(\epsilon) d\epsilon}{\sum_a N(\epsilon) d\epsilon}$$

where  $\epsilon$  was the energy level and  $N(\epsilon)$  is the number of orbitals at the energy level  $\epsilon$ . The parameters  $a$  and  $b$  were defined as the top or bottom limitation of the energy level for a certain orbital.

## 3. Results

### 3.1 Phase and structural characterization

The XRD spectra were obtained to identify the crystalline structure of  $\text{Ti}_3\text{AlC}_2$ ,  $\text{Ti}_3\text{C}_2$  MXene,  $\text{Co}^{2+}@ \text{Ti}_3\text{C}_2$  MXene and

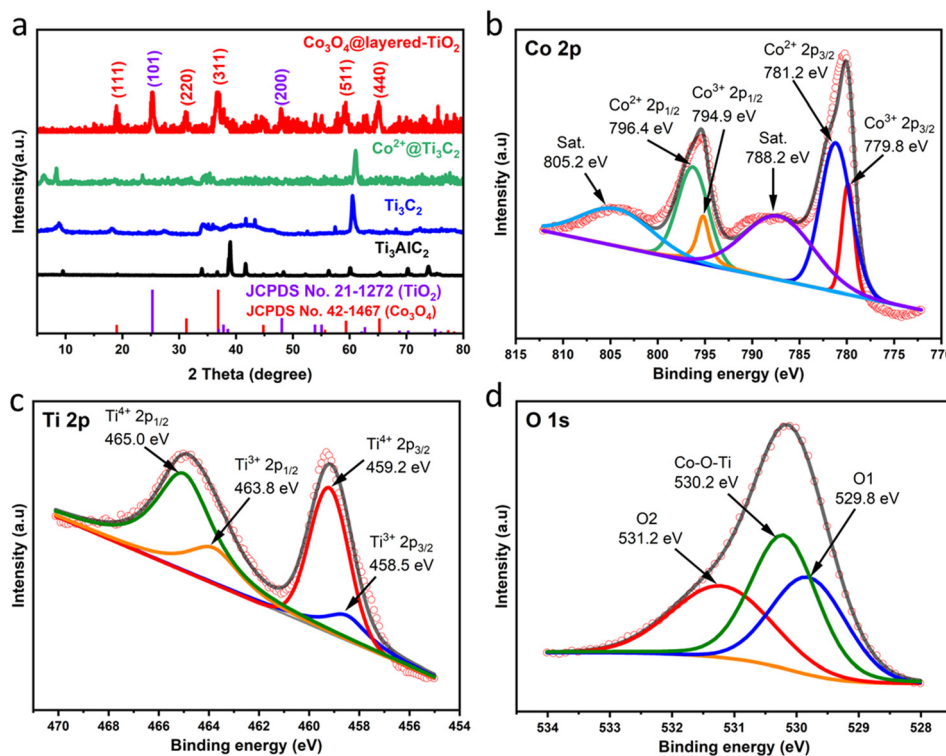


Fig. 2 (a) XRD patterns of  $\text{Ti}_3\text{AlC}_2$  (black),  $\text{Ti}_3\text{C}_2$  (blue),  $\text{Co}^{2+}@ \text{Ti}_3\text{C}_2$  (green) and  $\text{Co}_3\text{O}_4@ \text{layered-TiO}_2$  (red). The XRD standard card data for  $\text{TiO}_2$  (JCPDS no. 21-1272) and  $\text{Co}_3\text{O}_4$  (JCPDS no. 42-1467) are marked in purple and red. High-resolution XPS spectra of (b) Co 2p, (c) Ti 2p and (d) O 1s of  $\text{Co}_3\text{O}_4@ \text{layered-TiO}_2$ .



$\text{Co}_3\text{O}_4$ @layered- $\text{TiO}_2$  (Fig. 2a). After HF etching, the peak located at  $38.8^\circ$  related to Al of  $\text{Ti}_3\text{AlC}_2$  disappeared, and a new (002) peak of layered  $\text{Ti}_3\text{C}_2$  MXene appeared at  $8.8^\circ$ , indicating that the Al layer of the  $\text{Ti}_3\text{AlC}_2$  was successfully removed.<sup>27,28</sup> Compared with a previous work, which reported  $\text{Co}^{2+}$  through solvothermal treatment in ethanol to get  $\text{Co}_3\text{O}_4$  anchored on the surface of  $\text{Ti}_3\text{C}_2$  MXene nanosheets, in this case, after hydrothermal reaction, the precursor of  $\text{Co}^{2+}$  grown on the surface of layered  $\text{Ti}_3\text{C}_2$  MXene was not cobalt oxide.<sup>17</sup> This is because the coordination of cobalt ions with trans-1,4-cyclohexanedicarboxylic acid in DMF solution can inhibit the oxidation of cobalt ions in the formation of  $\text{Co}_3\text{O}_4$ . The obtained precursor of  $\text{Co}^{2+}$  on  $\text{Ti}_3\text{C}_2$  MXene facilitates the formation of covalent metal–oxygen bonds between metal oxides (cobalt oxide and titanium oxide) during the subsequent simultaneous oxidation process. The (002) peak of  $\text{Ti}_3\text{C}_2$  MXene related to interlayer spacing was downshifted to  $8.3^\circ$ , which indicates that the interlayer spacing was expanded after the precursor of  $\text{Co}^{2+}$  grew. Besides, the other peaks of  $\text{Ti}_3\text{C}_2$  MXene became weak and even vanished, which is attributed to a large amount of amorphous precursor of  $\text{Co}^{2+}$  covered on the surface of layered  $\text{Ti}_3\text{C}_2$  MXene. The diffraction peaks at  $19.0^\circ$ ,  $31.27^\circ$ ,  $36.85^\circ$ ,  $59.35^\circ$  and  $65.23^\circ$  can be well assigned to the (111), (220), (311), (511) and (440) lattice planes of  $\text{Co}_3\text{O}_4$  (JCPDS no. 42-1467), respectively. In addition, the diffraction peaks at  $25.28^\circ$ ,  $36.94^\circ$ ,  $37.8^\circ$ ,  $38.57^\circ$ ,  $48.04^\circ$ ,  $53.89^\circ$  and  $55.06^\circ$  can be well indexed to the (101), (103), (004), (112), (200), (105) and (211) lattice planes of  $\text{TiO}_2$  (JCPDS no. 21-1272), respectively.<sup>29,30</sup> No other impure diffraction peaks of metallic cobalt oxide were detected, indicating that pure phases of  $\text{TiO}_2$  and  $\text{Co}_3\text{O}_4$  were formed in  $\text{Co}_3\text{O}_4$ @layered- $\text{TiO}_2$ . Besides, the weak diffraction peak at  $8.3^\circ$  that corresponds to the (002) crystal plane of  $\text{Ti}_3\text{C}_2$  MXene disappeared, which is ascribed to the oxidation of  $\text{Ti}_3\text{C}_2$  MXene into  $\text{TiO}_2$  during annealing. The successful preparation of layered- $\text{TiO}_2$  and  $\text{Co}_3\text{O}_4$  was confirmed by XRD spectra (Fig. S1 and S2†).

XPS further determined the chemical state of the surface elements of  $\text{Co}_3\text{O}_4$ @layered- $\text{TiO}_2$ . The XPS survey spectra intuitively show that the Co, O and Ti elements exist in  $\text{Co}_3\text{O}_4$ @layered- $\text{TiO}_2$ . The intensity of the C element becomes negligible, which confirms that  $\text{Ti}_3\text{C}_2$  MXene was completely converted into  $\text{TiO}_2$  during the annealing treatment (Fig. S3†). In the Co 2p spectrum, the two peaks at 779.8 and 794.9 eV are attributed to the  $2p_{3/2}$  and  $2p_{1/2}$  peaks of  $\text{Co}^{3+}$  in  $\text{Co}_3\text{O}_4$ , respectively (Fig. 2b). Besides, the two peaks at 781.2 and 796.4 eV are attributed to the  $2p_{3/2}$  and  $2p_{1/2}$  peaks of  $\text{Co}^{2+}$  in  $\text{Co}_3\text{O}_4$ , respectively.<sup>31</sup> In the Ti 2p spectrum, the two peaks are located at 459.2 and 465.0 eV, which correspond to  $2p_{3/2}$  and  $2p_{1/2}$  of  $\text{Ti}^{4+}$  of  $\text{TiO}_2$ , respectively (Fig. 2c).<sup>32,33</sup> In the O 1s spectrum, the strong peak at 529.8 eV is attributed to the O1 peak of the metal oxide, further demonstrating the existence of  $\text{TiO}_2$  and  $\text{Co}_3\text{O}_4$  in the  $\text{Co}_3\text{O}_4$ @layered- $\text{TiO}_2$  (Fig. 2d).<sup>13</sup> The O2 peak

at 531.2 eV is ascribed to the hydroxyl group attached to the surface of the  $\text{Co}_3\text{O}_4$ @layered- $\text{TiO}_2$ .<sup>34</sup> In addition, based on previously reported oxygen atoms bound to metal atoms, the peak at 530.2 eV is attributed to the Co–O–Ti covalent bond between  $\text{Co}_3\text{O}_4$  and the  $\text{TiO}_2$  substrate,<sup>24,33</sup> since the cobalt precursor ( $\text{Co}^{2+}$ ) on the surface of the layered  $\text{Ti}_3\text{C}_2$  MXene was converted into  $\text{Co}_3\text{O}_4$ . Simultaneously, the  $\text{Ti}_3\text{C}_2$  MXene was oxidized into  $\text{TiO}_2$ , and the oxidation process promotes the formation of Co–O–Ti bonds.

The SEM image of  $\text{Ti}_3\text{AlC}_2$  exhibits a tightly stacked bulk structure (Fig. 3a). After removing the Al layer by HF etching,  $\text{Ti}_3\text{C}_2$  MXene with a layered structure was successfully prepared (Fig. 3b). Through hydrothermal treatment of  $\text{Ti}_3\text{C}_2$  MXene,  $\text{Co}^{2+}$  and trans-1,4-cyclohexanedicarboxylic acid, the interlayers of  $\text{Ti}_3\text{C}_2$  MXene were filled by the precursor of  $\text{Co}^{2+}$  (Fig. 3c). Finally, the precursor of  $\text{Co}^{2+}$  was successfully transformed to  $\text{Co}_3\text{O}_4$  nanoparticles by annealing in air. The  $\text{Co}_3\text{O}_4$  nanoparticles are uniformly grown on the surface of layered  $\text{TiO}_2$  (Fig. 3d). Besides, the  $\text{Co}_3\text{O}_4$ @layered- $\text{TiO}_2$  maintains the layered structure of  $\text{Ti}_3\text{C}_2$  MXene. Additionally, layered- $\text{TiO}_2$  obtained by direct oxidation of  $\text{Ti}_3\text{C}_2$  MXene also exhibits a layered structure (Fig. S4†).  $\text{Co}_3\text{O}_4$  prepared without MXene as a substrate exhibits a disordered filamentous structure (Fig. S5†). The crystal structure of  $\text{Co}_3\text{O}_4$ @layered- $\text{TiO}_2$  was further analyzed by TEM measurements. A large number of  $\text{Co}_3\text{O}_4$  nanoparticles uniformly anchored on the surface of layered  $\text{TiO}_2$  can be observed, which is consistent with SEM results (Fig. 3e). The average size of  $\text{Co}_3\text{O}_4$  nanoparticles was determined to be 20.68 nm by statistical analysis of particle size distribution (Fig. S6†). In the HR-TEM image, the lattice of  $\text{Co}_3\text{O}_4$  can be carefully recognized by a typical lattice distance of 0.46 nm corresponding to the (111) face of  $\text{Co}_3\text{O}_4$  (Fig. 3f and S7†).<sup>35,36</sup> In addition, the SAED pattern also confirmed that  $\text{Co}_3\text{O}_4$  and  $\text{TiO}_2$  exist in  $\text{Co}_3\text{O}_4$ @layered- $\text{TiO}_2$  (Fig. S8 and S9†). Consequently, the *in situ* formation of  $\text{Co}_3\text{O}_4$  nanoparticles attached to the surface of the layered  $\text{TiO}_2$  substrate was successfully identified. The elemental mapping images reveal that the Ti, Co and O elements were uniformly distributed in the  $\text{Co}_3\text{O}_4$ @layered- $\text{TiO}_2$  (Fig. 3g). Furthermore, the EDX image indicates that Co is the primary element on the surface of  $\text{Co}_3\text{O}_4$ @layered- $\text{TiO}_2$  (Fig. S10†).

### 3.2 Electrocatalytic performance of the OER

The OER performance of  $\text{Co}_3\text{O}_4$ @layered- $\text{TiO}_2$  was investigated in a typical three-electrode system with 1.0 M KOH as electrolyte. The  $\text{Co}_3\text{O}_4$ @layered- $\text{TiO}_2$  dispersion droplets on the surface of carbon paper serve as the working electrode. Besides, the Pt plate and the Hg/HgO electrode were used as counter and reference electrodes, respectively. For comparison,  $\text{Co}_3\text{O}_4$ , layered- $\text{TiO}_2$  and a commercial  $\text{RuO}_2$  catalyst was used as the contrast electrocatalysts, as presented by the LSV curves (Fig. 4a). Based on the EIS spectrum, LSV curves were corrected with 100% iR compensation (Fig. S11†). Compared to  $\text{Co}_3\text{O}_4$ , layered- $\text{TiO}_2$ ,  $\text{RuO}_2$  and carbon paper, the  $\text{Co}_3\text{O}_4$ @layered- $\text{TiO}_2$



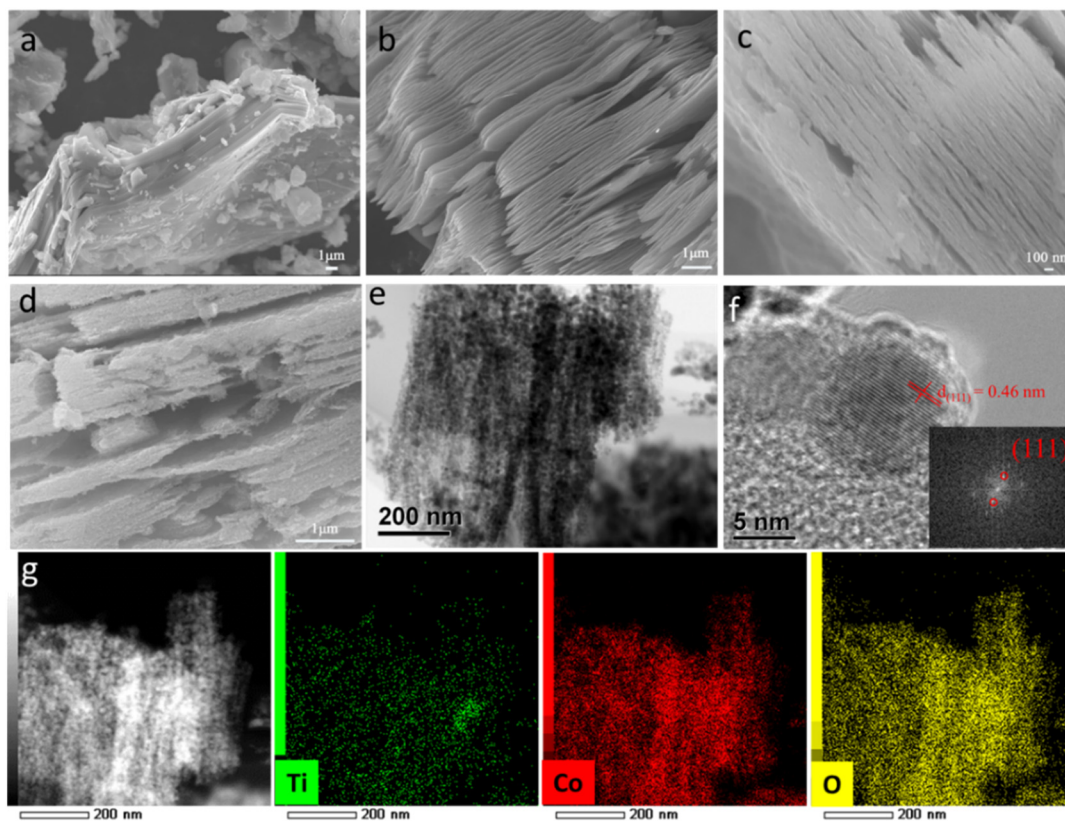


**Fig. 3** SEM images of (a)  $\text{Ti}_3\text{AlC}_2$ , (b)  $\text{Ti}_3\text{C}_2$  MXene, (c)  $\text{Co}^{2+}$ @ $\text{Ti}_3\text{C}_2$  MXene and (d)  $\text{Co}_3\text{O}_4$ @layered- $\text{TiO}_2$ . (e and f) TEM and HR-TEM images of  $\text{Co}_3\text{O}_4$ @layered- $\text{TiO}_2$  (the inset in Fig. 3f shows the fast fourier transform of the  $\text{Co}_3\text{O}_4$  crystal). (g) HAADF-STEM and elemental mapping images (Ti, Co and O) of  $\text{Co}_3\text{O}_4$ @layered- $\text{TiO}_2$  from left to right.

electrode exhibits the best OER performance, which can reach ampere-level current density with a small potential. It is worth

noting that the  $\text{Co}_3\text{O}_4$ @layered- $\text{TiO}_2$  electrode only requires a potential of 1.52 V and 1.60 V to reach a current density of 100

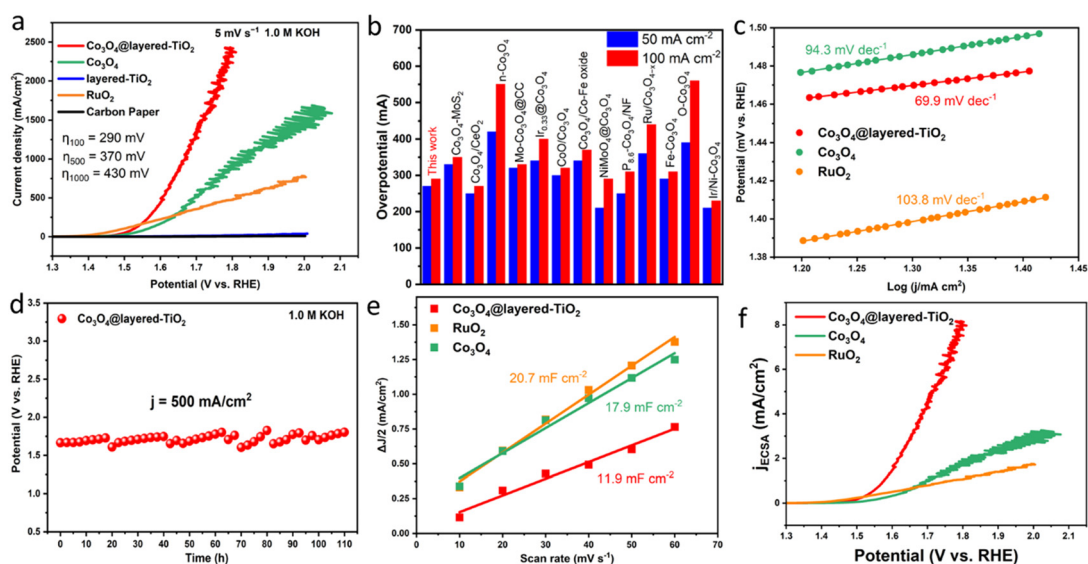


**Fig. 4** (a) OER LSV curves of  $\text{Co}_3\text{O}_4$ @layered- $\text{TiO}_2$ ,  $\text{Co}_3\text{O}_4$ , layered- $\text{TiO}_2$ ,  $\text{RuO}_2$  and carbon paper in 1.0 M KOH. (b) Overpotential comparison graph of  $\text{Co}_3\text{O}_4$ @layered- $\text{TiO}_2$  with  $\text{Co}_3\text{O}_4$ -based materials at  $50 \text{ mA cm}^{-2}$  and  $100 \text{ mA cm}^{-2}$ . (c) Tafel slope comparison graph of  $\text{Co}_3\text{O}_4$ @layered- $\text{TiO}_2$ ,  $\text{Co}_3\text{O}_4$  and  $\text{RuO}_2$ . (d) Galvanostatic measurement of  $\text{Co}_3\text{O}_4$ @layered- $\text{TiO}_2$  at  $500 \text{ mA cm}^{-2}$  for 110 h in 1.0 M KOH. (e) The plots of current density versus the scan rates of 10, 20, 30, 40, 50 and  $60 \text{ mV s}^{-1}$ . (f) OER LSV curves of  $\text{Co}_3\text{O}_4$ @layered- $\text{TiO}_2$ ,  $\text{Co}_3\text{O}_4$  and  $\text{RuO}_2$  normalized by ECSA in 1.0 M KOH.



mA cm<sup>-2</sup> and 500 mA cm<sup>-2</sup>, respectively. In addition, it only needs 1.66 V to reach an ampere-level current density of 1000 mA cm<sup>-2</sup>. Besides, carbon paper shows negligible performance for the OER. Furthermore, the performance of Co<sub>3</sub>O<sub>4</sub>@layered-TiO<sub>2</sub> obtained after annealing at 300 °C is superior to that of Co<sub>3</sub>O<sub>4</sub>@layered-TiO<sub>2</sub> annealed at 250 °C and 350 °C (Fig. S12†). The results obtained at various current densities exhibit a superb low overpotential, which surpasses most of the previously reported literature on Co<sub>3</sub>O<sub>4</sub>-based catalysts (Fig. 4b and Table S1†). Furthermore, the Co<sub>3</sub>O<sub>4</sub>@layered-TiO<sub>2</sub> exhibits the smallest Tafel slope value of 69.9 mV dec<sup>-1</sup>, which is much smaller than 94.3 mV dec<sup>-1</sup> of Co<sub>3</sub>O<sub>4</sub> and 103.8 mV dec<sup>-1</sup> of RuO<sub>2</sub> (Fig. 4c). The results prove that the Co<sub>3</sub>O<sub>4</sub>@layered-TiO<sub>2</sub> has ultrafast kinetics for the OER due to the Co<sub>3</sub>O<sub>4</sub> nanoparticles supported on the TiO<sub>2</sub> substrate with Co–O–Ti covalent bonds.<sup>37</sup> More importantly, achieving the OER at high current density has always been a thorny problem. Therefore, galvanostatic measurement of half ampere-level current density was applied to demonstrate that the electrode meets industry requirements for catalytic OER stability. As a result, the Co<sub>3</sub>O<sub>4</sub>@layered-TiO<sub>2</sub> electrode can achieve long-term stability of the OER at 500 mA cm<sup>-2</sup> up to 110 h, which proves that the Co<sub>3</sub>O<sub>4</sub>@layered-TiO<sub>2</sub> has superb stability for the OER (Fig. 4d). In addition, the morphology of Co<sub>3</sub>O<sub>4</sub>@layered-TiO<sub>2</sub> after 110 hours of durability testing remains almost unchanged, proving that the electrode maintains excellent stability even after the high current density stability test (Fig. S13†).

The intrinsic catalytic activity was analyzed using electrochemically active surface areas (ECSAs) of different catalysts, estimated by a series of CV tests with various scan rates. The ECSA can be determined by  $ECSA = C_{dl}/C_s$ , where  $C_{dl}$  and  $C_s$  are the double-layer capacitance and the specific capacitance of the electrode, respectively.<sup>38–42</sup> In this work,  $C_s = 0.04$  mF cm<sup>-2</sup> was used as the value for the general specific capacitance based on the reported value.<sup>33</sup> The CV curves of Co<sub>3</sub>O<sub>4</sub>@layered-TiO<sub>2</sub>, Co<sub>3</sub>O<sub>4</sub> and RuO<sub>2</sub> under different scan speeds were tested (Fig. S14–S16†).  $C_{dl}$  was obtained by fitting  $\Delta J$  (half of the oxidation and reduction current density) values with different scan speeds of 10, 20, 30, 40, 50 and 60 mV s<sup>-1</sup> (Fig. 4e). As a result,  $C_{dl}$  of the Co<sub>3</sub>O<sub>4</sub>@layered-TiO<sub>2</sub> electrode exhibits an ECSA value of 11.9 mF cm<sup>-2</sup>. The ECSA of Co<sub>3</sub>O<sub>4</sub>@layered-TiO<sub>2</sub>, Co<sub>3</sub>O<sub>4</sub> and RuO<sub>2</sub> are 297.5, 447.5 and 517 cm<sup>2</sup>, respectively. After normalization of polarization curves by ECSA, it can be found that Co<sub>3</sub>O<sub>4</sub>@layered-TiO<sub>2</sub> still possesses the highest intrinsic catalytic activity toward the OER compared with Co<sub>3</sub>O<sub>4</sub> and RuO<sub>2</sub> (Fig. 4f). This result further proves that the Co<sub>3</sub>O<sub>4</sub> nanoparticles attached on the TiO<sub>2</sub> surface with Co–O–Ti covalent bonds possess the optimal intrinsic electrocatalytic activity for the OER in alkaline conditions.

### 3.3 Studies on the mechanism of catalytic activities

To investigate the origin of the remarkable OER performance of Co<sub>3</sub>O<sub>4</sub>@layered-TiO<sub>2</sub>, DFT simulations were carried out to confirm that the Co<sub>3</sub>O<sub>4</sub> nanoparticles attached on the surface of TiO<sub>2</sub> with Co–O–Ti covalent

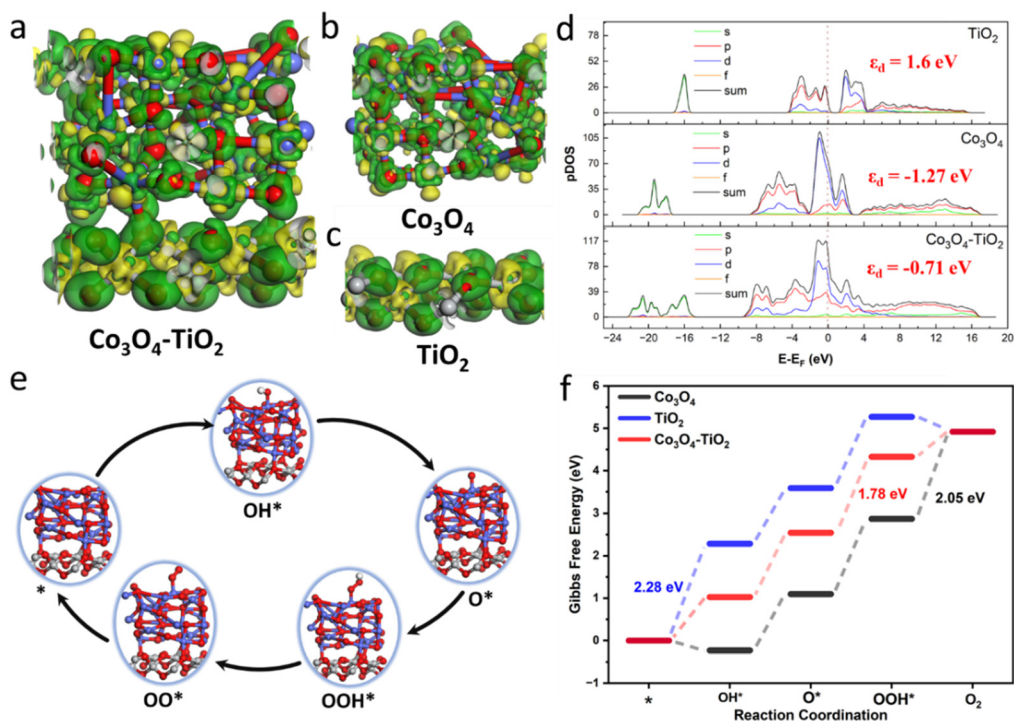


**Fig. 5** The side views of charge density difference of (a) Co<sub>3</sub>O<sub>4</sub>-TiO<sub>2</sub>, (b) Co<sub>3</sub>O<sub>4</sub> and (c) TiO<sub>2</sub>. Green indicates positive charges and yellow indicates negative charges. (d) Calculated DOS and d-band center ( $\epsilon_d$ ) of Co<sub>3</sub>O<sub>4</sub>-TiO<sub>2</sub>, Co<sub>3</sub>O<sub>4</sub> and TiO<sub>2</sub>. (e) Schematic illustration of the OER mechanisms. (f) Calculation of Gibbs free energy ( $\Delta G$ ) of each step of the OER and rate-determining step energy barriers of Co<sub>3</sub>O<sub>4</sub>-TiO<sub>2</sub>, Co<sub>3</sub>O<sub>4</sub> and TiO<sub>2</sub>.



bonds have high catalytic activity. The constructed model of  $\text{Co}_3\text{O}_4$  on  $\text{TiO}_2$  ( $\text{Co}_3\text{O}_4\text{-TiO}_2$ ) with Co–O–Ti bonds was utilized for adsorbing reaction intermediates (Fig. S17†). The charge density difference of  $\text{Co}_3\text{O}_4\text{-TiO}_2$  indicates that the attached  $\text{Co}_3\text{O}_4$  on the  $\text{TiO}_2$  can effectively regulate the charge redistribution, where the  $\text{Co}_3\text{O}_4$  and  $\text{TiO}_2$  tend to lose electrons, and the delocalized electrons accumulate around the adjacent Co–O–Ti bonds. (Fig. 5a–c).<sup>43</sup> The d-band center ( $\varepsilon_d$ ) often dominates the progress of electrochemical reactions because it is directly related to the adsorption strength of the catalyst to reaction intermediates. According to the projected density of states (pDOS), it has been observed that attaching  $\text{Co}_3\text{O}_4$  on the  $\text{TiO}_2$  surface tends to alter  $\varepsilon_d$  (Fig. 5d). In here, the  $\varepsilon_d$  value of  $\text{TiO}_2\text{-Co}_3\text{O}_4$  is closer to the Fermi level (–0.71 eV) than  $\varepsilon_d$  of  $\text{TiO}_2$  and  $\text{Co}_3\text{O}_4$ , which is advantageous in regulating the adsorbed intermediates on the catalyst surface.<sup>25,44,45</sup> Additionally, in  $\text{TiO}_2\text{-Co}_3\text{O}_4$ , the total density of states (TDOS) at the Fermi level is increased, confirming that attaching  $\text{Co}_3\text{O}_4$  to  $\text{TiO}_2$  can enhance the conductivity of  $\text{Co}_3\text{O}_4$  and  $\text{TiO}_2$ . The performance of the OER was determined by calculating Gibbs free energy of reaction condonation of \*OH, \*O, and \*OOH steps (Fig. 5e). The structural model has been optimized after adsorbing OH, O, and OOH on the Co site of  $\text{TiO}_2\text{-Co}_3\text{O}_4$  (Fig. S18–S20†). As a result, the rate-determining step (RDS) energy barriers of  $\text{Co}_3\text{O}_4$ ,  $\text{TiO}_2$  and  $\text{Co}_3\text{O}_4\text{-TiO}_2$  are 2.05, 2.28 and 1.78 eV, respectively. The RDS of  $\text{Co}_3\text{O}_4\text{-TiO}_2$  (\*O + OH<sup>–</sup> → \*OOH + e<sup>–</sup>) has a low free energy barrier of 1.78 eV, which is beneficial to accelerate the OER processes (Fig. 5f). This result demonstrates that the attachment of  $\text{Co}_3\text{O}_4$  on the  $\text{TiO}_2$  surface with Co–O–Ti covalent bonds is beneficial for reducing the energy barrier for the OER, thus boosting OER performance at ampere-level current density.

## 4. Conclusions

$\text{Co}_3\text{O}_4$  nanoparticles supported on the  $\text{TiO}_2$  surface with Co–O–Ti covalent bonds were constructed. When the cobalt precursor ( $\text{Co}^{2+}$ ) on the surface of the layered  $\text{Ti}_3\text{C}_2$  MXene was converted into  $\text{Co}_3\text{O}_4$ , the  $\text{Ti}_3\text{C}_2$  MXene was also oxidized into  $\text{TiO}_2$ , which promotes the formation of Co–O–Ti bonds. As a result,  $\text{Co}_3\text{O}_4@\text{layered-TiO}_2$  exhibits brilliant OER performance with ultra-low potential, ampere-level current density and long-term durability. When the current density reaches 100 mA cm<sup>–2</sup> and 1000 mA cm<sup>–2</sup>, the required potential is only 1.52 V and 1.66 V, respectively. Additionally, it can achieve long-term stability up to 110 h at 500 mA cm<sup>–2</sup>. DFT studies have demonstrated that the Co–O–Ti covalent bond between  $\text{Co}_3\text{O}_4$  and  $\text{TiO}_2$  can adjust the d-band center, which is beneficial for reducing the energy barrier for intermediates of the OER. This result illuminates a new strategy of using metal oxide substrates to support active materials for highly efficient electrocatalysis.

## Data availability statement

The original data are available from the corresponding author on reasonable request.

## Author contributions

Hong Tang: conceptualization, data curation, formal analysis, investigation, methodology, validation, visualization, and writing – original draft. Wei Wu: validation and visualization. Takahiro Kojima: visualization and writing – review & editing. Kenji Kazumi: resources. Kazuhiro Fukami: resources and writing – review & editing. Hiroshi Sakaguchi: funding acquisition, project administration, supervision, and writing – review & editing.

## Conflicts of interest

There are no conflicts to declare.

## Acknowledgements

This study was supported by the KAKENHI Program No. 22H01891 (H. S.), 22K18944 (H. S.), 23K04521 (T. K.), the Japan Society for the Promotion of Science, Japan; the Zero-Emission Energy Research (ZE2022B-07), IAE, Kyoto University (K. F.); Hong Tang thanks the China Scholarship Council (CSC) for the financial support.

## References

- 1 S. Zhang, C. Tan, R. Yan, X. Zou, F. Hu, Y. Mi, C. Yan and S. Zhao, *Angew. Chem., Int. Ed.*, 2023, **62**, 202302795.
- 2 M. G. Kim, T. K. Lee, E. Lee, S. Park, H. J. Lee, H. Jin, D. W. Lee, M. G. Jeong, H. G. Jung, K. Im, C. Hu, H. C. Ham, K. H. Song, Y. E. Sung, Y. M. Lee and S. J. Yoo, *Energy Environ. Sci.*, 2023, **16**, 5019–5028.
- 3 A. M. Idris, S. Zheng, M. Zhang, X. Jiang, G. Jiang, J. Wang, S. Li and Z. Li, *Catal. Sci. Technol.*, 2023, **13**, 6456–6462.
- 4 S. Gao, L. Wang, X. Kang, L. Wang, X. Duan and W. Wang, *Catal. Sci. Technol.*, 2024, **14**, 1349–1358.
- 5 S. Li, J. Wang, X. Lv, S. Zheng, J. Wang and Z. Li, *Catal. Sci. Technol.*, 2023, **13**, 1512–1517.
- 6 T. Guo, L. Li and Z. Wang, *Adv. Energy Mater.*, 2022, **12**, 2200827.
- 7 S. Chandrasekaran, M. Khandelwal, F. Dayong, L. Sui, J. S. Chung, R. D. K. Misra, P. Yin, E. J. Kim, W. Kim, A. Vanchiappan, Y. Liu, S. H. Hur, H. Zhang and C. Bowen, *Adv. Energy Mater.*, 2022, **12**, 2200409.
- 8 M. Li, X. Wang, K. Liu, H. Sun, D. Sun, K. Huang, Y. Tang, W. Xing, H. Li and G. Fu, *Adv. Mater.*, 2023, **35**, 2302462.
- 9 Z. Pei, H. Tan, J. Gu, L. Lu, X. Zeng, T. Zhang, C. Wang, L. Ding, P. J. Cullen, Z. Chen and S. Zhao, *Nat. Commun.*, 2023, **14**, 818.
- 10 Y. Liu, Z. Jiang and Z. J. Jiang, *Adv. Funct. Mater.*, 2023, **33**, 2302883.



- 11 X. Li, J. Huang, Z. Liu, Q. Chen, G. Chen, Y. Zhang, K. Kajiyoshi, Y. Zhao, Y. Liu, L. Cao and L. Feng, *Catal. Sci. Technol.*, 2023, **13**, 6550–6560.
- 12 R. Luo, Z. Qian, L. Xing, C. Du, G. Yin, S. Zhao and L. Du, *Adv. Funct. Mater.*, 2021, **31**, 2102918.
- 13 P. Wang, T. Yu, L. Hao and X. Liu, *J. Power Sources*, 2024, **589**, 233749.
- 14 Y. Huang, M. Li, F. Pan, Z. Zhu, H. Sun, Y. Tang and G. Fu, *Carbon Energy*, 2022, **5**, 279.
- 15 Y. F. Cui, S. D. Jiang, Q. Fu, R. Wang, P. Xu, Y. Sui, X. J. Wang, Z. L. Ning, J. F. Sun, X. Sun, A. Nikiforov and B. Song, *Adv. Funct. Mater.*, 2023, **33**, 2306889.
- 16 E. M. Davis, A. Bergmann, C. Zhan, H. Kuhlbeck and B. R. Cuenya, *Nat. Commun.*, 2023, **14**, 4791.
- 17 Y. Lu, D. Fan, Z. Chen, W. Xiao, C. Cao and X. Yang, *Sci. Bull.*, 2020, **65**, 460–466.
- 18 Z. Liu, M. Corva, H. M. A. Amin, N. Blanc, J. Linnemann and K. Tschulik, *Int. J. Mol. Sci.*, 2021, **22**, 13137.
- 19 A. Wang, W. Wang, J. Xu, A. Zhu, C. Zhao, M. Yu, G. Shi, J. Yan, S. Sun and W. Wang, *Adv. Energy Mater.*, 2023, **13**, 2302537.
- 20 C. Yang, Z. Wu, Z. Zhao, Y. Gao, T. Ma, X. Luo, C. Cheng, Y. Wang, S. Li and C. Zhao, *Adv. Mater.*, 2023, **35**, 2303331.
- 21 X. Zheng, X. Shi, H. Ning, R. Yang, B. Lu, Q. Luo, S. Mao, L. Xi and Y. Wang, *Nat. Commun.*, 2023, **14**, 4209.
- 22 C. Li, S. H. Kim, H. Y. Lim, Q. Sun, Y. Jiang, H. J. Noh, S. J. Kim, J. Baek, S. K. Kwak and J. B. Baek, *Adv. Mater.*, 2023, **35**, 2301369.
- 23 Y. Zhu, J. Wang, T. Koketsu, M. Kroschel, J. M. Chen, S. Y. Hsu, G. Henkelman, Z. Hu, P. Strasser and J. Ma, *Nat. Commun.*, 2022, **13**, 7754.
- 24 X. Zheng, L. Li, M. Deng, J. Li, W. Ding, Y. Nie and Z. Wei, *Catal. Sci. Technol.*, 2020, **10**, 4743–4751.
- 25 D. C. Nguyen, T. L. Luyen Doan, S. Prabhakaran, D. T. Tran, D. H. Kim, J. H. Lee and N. H. Kim, *Nano Energy*, 2021, **82**, 105750.
- 26 R. Vadakkekara, R. Illathvalappil and S. Kurungot, *ChemElectroChem*, 2018, **5**, 4000–4007.
- 27 R. Zhang, L. Pan, B. Guo, Z. F. Huang, Z. Chen, L. Wang, X. Zhang, Z. Guo, W. Xu, K. P. Loh and J. J. Zou, *J. Am. Chem. Soc.*, 2023, **145**, 2271–2281.
- 28 H. Tang, R. Guo, M. Jiang, Y. Zhang, X. Lai, C. Cui, H. Xiao, S. Jiang, E. Ren and Q. Qin, *J. Power Sources*, 2020, **462**, 228152.
- 29 A. Zaka, M. A. Mansoor, M. A. Asghar, A. Haider and M. Iqbal, *Int. J. Hydrogen Energy*, 2023, **48**, 34599–34609.
- 30 L. Deng, B. Chang, D. Shi, X. Yao, Y. Shao, J. Shen, B. Zhang, Y. Wu and X. Hao, *Renewable Energy*, 2021, **170**, 858–865.
- 31 Z. Zhao, M. Yu, Y. Liu, T. Zeng, R. Ye, Y. Liu, J. Hu and A. Li, *Adv. Energy Sustainability Res.*, 2023, **4**, 2300123.
- 32 C. E. Park, G. H. Jeong, J. Theerthagiri, H. Lee and M. Y. Choi, *ACS Nano*, 2023, **17**, 7539–7549.
- 33 L. Zhou, Y. Shao, F. Yin, J. Li, F. Kang and R. Lv, *Nat. Commun.*, 2023, **14**, 7644.
- 34 Z. Liu, H. M. A. Amin, Y. Peng, M. Corva, R. Pentcheva and K. Tschulik, *Adv. Funct. Mater.*, 2023, **33**, 2210945.
- 35 C. Alex, S. C. Sarma, S. C. Peter and N. S. John, *ACS Appl. Energy Mater.*, 2020, **3**, 5439–5447.
- 36 C. Z. Yuan, S. Wang, K. San Hui, K. Wang, J. Li, H. Gao, C. Zha, X. Zhang, D. A. Dinh, X. L. Wu, Z. Tang, J. Wan, Z. Shao and K. N. Hui, *ACS Catal.*, 2023, **13**, 2462–2471.
- 37 G. Li, H. Jang, S. Liu, Z. Li, M. G. Kim, Q. Qin, X. Liu and J. Cho, *Nat. Commun.*, 2022, **13**, 1270.
- 38 D. H. Wu, M. Ul Haq, L. Zhang, J. J. Feng, F. Yang and A. J. Wang, *J. Colloid Interface Sci.*, 2024, **662**, 149–159.
- 39 M. Ul Haq, D. H. Wu, Z. Ajmal, Q. D. Ruan, S. Khan, L. Zhang, A. J. Wang and J. J. Feng, *Appl. Catal., B*, 2024, **344**, 123632.
- 40 L. Zhang, L. L. Liu, J. J. Feng and A. J. Wang, *J. Colloid Interface Sci.*, 2024, **661**, 102–112.
- 41 Z. Ge, Y. Ding, T. Wang, F. Shi, P. Jin, P. Chen, B. He, S. Yin and Y. Chen, *J. Energy Chem.*, 2023, **77**, 209–216.
- 42 X. Liu, Y. Jiang, J. Huang, W. Zhong, B. He, P. Jin and Y. Chen, *Carbon Energy*, 2023, **5**, 367.
- 43 X. Song, H. Yang, C. Zhang, G. Zhang, H. Wu, Y. He, M. Fu, X. Liu, S. Li and S. Wei, *Catal. Sci. Technol.*, 2024, **14**, 735–745.
- 44 Y. Li, T. Xu, Q. Huang, L. Zhu, Y. Yan, P. Peng and F. F. Li, *ACS Catal.*, 2023, **13**, 7597–7605.
- 45 Y. Zhang, C. Ma, X. Zhu, K. Qu, P. Shi, L. Song, J. Wang, Q. Lu and A. Wang, *Adv. Energy Mater.*, 2023, **13**, 2301492.

